Johann Radon Institute for
Computational and Applied Mathematics
Austrian Academy of Sciences (ÖAW)

Inverse acoustic obstacle scattering problems using multifrequency measurements

M. Sini, T.T. Nguyen

RICAM-Report 2011-28

Inverse acoustic obstacle scattering problems using multifrequency measurements

Mourad Sini and Nguyen Trung Thành
Johann Radon Institute for Computational and Applied Mathematics (RICAM),
Austrian Academy of Sciences
Altenbergerstrasse 69, A-4040 Linz, Austria
Email addresses: mourad.sini@oeaw.ac.at, trung-thanh.nguyen@oeaw.ac.at

October 13, 2011

Abstract

In this paper, we investigate the problem of reconstructing sound-soft acoustic obstacles using multifrequency far field measurements corresponding to one direction of incidence. The idea is to obtain a rough estimate of the obstacle's shape at the lowest frequency using the least-squares approach, then refine it using a recursive linearization algorithm at higher frequencies. Using this approach, we show that an accurate reconstruction can be obtained without requiring a good initial guess. The analysis is divided into three steps. Firstly, we give a quantitative estimate of the domain of local convexity of the least-squares objective functional at the lowest frequency. This result enables us to obtain a rough approximation of the obstacle at the lowest frequency from any initial guess in this convex domain using gradient-based iterative procedures. Secondly, we describe the recursive linearization algorithm and analyze its convergence for noisy data. We qualitatively explain the relationship between the noise level and the resolution limit of the reconstruction. Thirdly, we justify a conditional asymptotic Lipschitz stability estimate of the illuminated part of the obstacle at high frequencies. The performance of the algorithm is illustrated with numerical examples.

Keywords: Inverse obstacle scattering, multifrequency, recursive linearization algorithm, convergence, high frequency stability.

AMS classification codes: 35R30, 65N21, 78A46.

1 Introduction

The main objective of inverse obstacle scattering problems is to reconstruct the shape and/or physical properties of penetrable or impenetrable obstacles using the scattering theory of waves, for example acoustic, electromagnetic or elastic waves. Its applications can be found in several fields such as nondestructive evaluations, medical imaging, geophysics and remote sensing. In

these problems, incident waves are sent and the waves scattered by the obstacles are measured either near (near field measurements) or far away (far field measurements) from the obstacles. In the literature, different methods have been used to solve the inverse scattering problems, depending on the types of measurements. For methods applied to measurements at a fixed frequency, we refer the reader to [6, 10, 20, 23] and the references therein.

In this work, we consider the problem of reconstructing the shape of a sound-soft acoustic obstacle using far field measurements associated with incident plane waves sent from only one incident direction but at multiple frequencies. Using only one incident direction makes this type of measurements very feasible in practice, especially when it is not possible or too time-consuming to perform the data acquisition for many different incident directions. The motivation for using multifrequency data is explained as follows. On the one hand, at low frequencies, we know that the reconstruction problem is uniquely solvable, see [11], but its stability is poor (only of *log-type*), see [18, 25]. That means, at low frequencies, it is difficult to reconstruct small details of the obstacle. On the other hand, at high frequencies, this inverse problem may not be uniquely solvable but it is more stable (see section 5).

To take the advantages of both low and high frequencies, we use the following approach. We first use the data at the lowest frequency to reconstruct a rough approximation of the obstacle's shape by minimizing the least-squares objective functional. Then, we refine the reconstruction by using recursive optimization methods at higher frequencies. As shown in the next sections, this approach enables us to obtain an accurate reconstruction of the part of the obstacle's boundary illuminated by the incident plane waves without requiring a good initial guess. The analysis of this approach is divided into three steps.

In the first step, we investigate the behavior of the least-squares objective functional at the lowest frequency. More precisely, we derive a quantitative estimate of the set of local convexity of the objective functional at a fixed frequency, see Theorem 3.2. Our analysis shows that, the size of this set is inversely proportional to the used frequency, i.e., the smaller the frequency, the larger the set of convexity. As a consequence, if the obstacle is expected to be contained in a known domain, the lowest frequency should be chosen small enough so that the set of convexity of the objective functional contains this domain. Then any shape in this domain can be used as an initial guess to obtain an approximation of the obstacle's shape due to the convexity of the objective functional. The proof of this result is based on the quantitative uniqueness results of Colton and Sleeman [11], see also Gintides [13], and the injectivity of the domain derivative of the far field operator which maps the obstacle's shape to the far field pattern of the scattered wave.

The appropriate choice of the lowest frequency avoids the need of a good initial guess to obtain an approximation of the true shape. However, due to the lack of good stability at low frequencies, we can only expect a rough approximation (e.g., we may obtain only an approximation of the obstacle's size). To increase the accuracy, our idea is then to use this rough approximation as an initial guess for minimizing the objective functional at a higher frequency.

For this purpose, we make use of recursive optimization methods. The second step is devoted to the convergence of the recursive optimization algorithms. As an example, we use a recursive linearization algorithm (RLA) which was proposed by Chen [7] for the inhomogeneous medium problem. The idea of this algorithm is to replace the nonlinear least-squares objective functional at each frequency by a linearized one using the Taylor expansion at the solution at a lower frequency. The linear convergence of this algorithm was first proved by Bao and Triki in [4] for the inhomogeneous medium problem in the case of noiseless data. Following the same techniques as [4], we also prove the linear convergence of the RLA for the obstacle problem with the presence of noise, see Theorem 4.5. We should emphasize that, unlike the noiseless case of [4], we show that a condition relating the noise level and the resolution limit of the reconstruction must be satisfied in order to guarantee the convergence of the algorithm (see Remark 4.3). In the proof, we also simplify some arguments and hypotheses of [4]. Note that other recursive optimization methods, such as the second order approximation or fully nonlinear recursive algorithm, are possible instead of the RLA, see, e.g., [5, 9].

The approximation at the highest frequency is considered as the reconstruction of the obstacle's shape using this type of algorithms. To understand its accuracy, in the third step, we discuss the stability at high frequencies. In this part, an asymptotic expansion of the far field pattern with respect to frequency obtained by Gutman and Ramm [14] is used. The asymptotic expansion represents the far field pattern as a function of the curvature and the so-called support function of the obstacle at high frequencies. We justify a conditional asymptotic Lipschitz stability estimate of the support function on the part of the obstacle's boundary illuminated by the incident wave, see Theorem 5.2. This result explains why we can reconstruct small details of the illuminated part at high frequencies.

The rest of the paper is organized as follows. In section 2, we state the forward and inverse problems under investigation. Section 3 is devoted to the analysis of the reconstruction problem at the lowest frequency. In section 4 we recall the RLA and discuss its convergence. The high frequency stability estimate is given in section 5. In section 6, we show numerical results to illustrate the performance of the method. Finally, we draw some conclusions and perspectives in section 7.

2 Problem statement

We consider the scattering of time-harmonic acoustic waves by a two-dimensional sound-soft obstacle $D \subset \mathbb{R}^2$. The total field u associated with an incident wave u^i can be represented as the solution to the following two-dimensional Dirichlet boundary value problem [10]

$$\Delta u(x) + k^2 u(x) = 0, \ x \in \mathbb{R}^2 \setminus \bar{D}, \tag{1}$$

$$u(x) = 0, \ x \in \partial D, \tag{2}$$

$$\lim_{|x|\to\infty} \sqrt{|x|} \left[\frac{\partial u^s(x)}{\partial |x|} - iku^s(x) \right] = 0, \tag{3}$$

where k is the wavenumber and $u^s := u - u^i$ is the scattered field. In the above system, the incident wave u^i is assumed to satisfy the equation $\Delta u^i(x) + k^2 u^i(x) = 0,\ x \in \mathbb{R}^2$. The equation (3) is called the Sommerfeld radiation condition, which guarantees the unique solvability of the problem (1)–(2).

The well-posedness of the problem (1)–(3) is well-known under the assumption that ∂D is Lipschitz (see, e.g., [22]). Moreover, the asymptotic behavior of the scattered field u^s at infinity can be represented by

$$u^s(x) = \frac{e^{ik|x|}}{\sqrt{|x|}} u^\infty(\hat{x}) + O(|x|^{-3/2}),\ |x| \to \infty, \tag{4}$$

where $\hat{x} := x/|x|$ and u^∞ is an analytic function on the unit circle $\mathbb{S}^1 := \{x \in \mathbb{R}^2 : |x| = 1\}$ referred to as the *far field pattern* of the scattered field u^s.

In this work, we make use of incident plane waves of the form $u^i(x) := e^{ikx\cdot\theta}$, with $\theta \in \mathbb{S}^1$ being a fixed direction of incidence. The inverse problem we investigate here is *to reconstruct the obstacle D from measured far field patterns $u^\infty(\hat{x}, k),\ \hat{x} \in \mathbb{S}^1$, for **one** direction of incidence $\theta \in \mathbb{S}^1$ and multiple wavenumbers k in the interval $[k_l, k_h]$*. Here k_l and k_h satisfy the condition $0 < k_l < k_h$ and we denote the far field pattern by $u^\infty(\hat{x}, k)$ to emphasize its dependence on the wavenumber k.

The uniqueness of this inverse problem is known in the literature if a band of wavenumbers $[k_l, k_h]$ is used, see, e.g., [24]. For a finite number of wavenumbers, as we consider in this paper, the uniqueness is guaranteed if the lowest frequency is small enough, see, e.g., [11, 13]. For local uniqueness at each frequency, see [26]. In the case that we have more *a priori* information about the obstacle's shape, some global uniqueness results at an arbitrary but fixed frequency have been published. For example, if the obstacle is polygonal, see [2, 8] and if the obstacle is nowhere analytic, see [16]. Regarding the stability issue, *loglog* stability estimates are given in [18] and an improved *log* stability estimate is shown in [25].

To reconstruct the obstacle's shape using iterative algorithms, parametrization methods are usually required to represent the shape. One of the most common parametrization methods is to use harmonic expansions. For the sake of simplicity, we confine our investigation to the case of star-shaped obstacles. We note that, our analysis can also be applied to other types of shapes using, e.g., perturbation representations, see, e.g., [3, 21]. Under the assumption of star-shaped, the boundary of the obstacle D can be represented by the following formula in polar coordinates

$$\partial D = \{x(t) \in \mathbb{R}^2 : x(t) = x^0 + r(t)(\cos t, \sin t), t \in [0, 2\pi]\}, \tag{5}$$

where x^0 is a given internal point of D in $\mathbb{R}^2$ and the radial function r is positive in $[0, 2\pi]$ with $r(0) = r(2\pi)$. In the following, we denote by $D(r)$ to indicate the dependence of the obstacle on its radial function r. In this paper, we assume that the shape is of class C^3, i.e., $r \in C^3[0, 2\pi]$. We denote by $X := \{\varphi \in C^3[0, 2\pi] : \varphi(0) = \varphi(2\pi)\}$ and $X^+ := \{\varphi \in X : \varphi(t) > 0\ \forall t \in [0, 2\pi]\}$. It is clear that $r \in X^+$. The space X is equipped with the C^3-norm.

For each wavenumber k, we define the *far field operator* $F(\cdot,k)$ from X^+ to $Y := L^2(\mathbb{S}^1)$ which assigns each function $r \in X^+$ to the far field pattern $u^\infty(\cdot,k,r)$ of the forward scattering problem (1)–(3) with $D = D(r)$. The "domain derivative" of F at r in the direction $a \in X$ is defined by

$$\partial_r F(r,k)a := \lim_{\epsilon \searrow 0} \frac{F(r+\epsilon a,k) - F(r,k)}{\epsilon}.$$

We call $\partial_r F(r,k)$ the domain derivative of F at r. It is a linear operator from X to Y. The calculation of $\partial_r F(r,k)a$ is given in the following theorem, which was proved by Kirsch, see [19].

Theorem 2.1. *Let $r \in X^+$, $a \in X$ and u be the total field of the problem (1)–(3) with $D = D(r)$. Then the domain derivative $\partial_r F(r,k)a$ exists and is given by*

$$\partial_r F(r,k)a = \tilde{u}^\infty,$$

where $\tilde{u}^\infty$ is the far field pattern of the following problem

$$\Delta \tilde{u}(x) + k^2 \tilde{u}(x) = 0, x \in \mathbb{R}^2 \setminus \bar{D}, \tag{6}$$

$$\tilde{u}(x(t)) = -a(t)(\cos t, \sin t) \cdot \nu(x(t)) \frac{\partial u(x(t))}{\partial \nu}, x(t) \in \partial D, t \in [0, 2\pi], \tag{7}$$

$$\lim_{|x| \to \infty} \sqrt{|x|} \left[\frac{\partial \tilde{u}(x)}{\partial |x|} - ik\tilde{u}(x) \right] = 0, \tag{8}$$

with $\nu(x)$ being the outward unit normal vector at $x \in \partial D$.

The following lemma, which is a consequence of Theorem 2.1, plays a crucial role in estimating the domain of local convexity in Section 3 as well as the convergence analysis of the RLA in Section 4.2. For its proof, see [19, 21].

Lemma 2.2. *For each $r \in X^+$, the domain derivative $\partial_r F(r,k)$ is an injective linear operator from X to Y.*

Remark 2.1. *Theorem 2.1 and Lemma 2.2 are also valid for domains of class C^2, see [19]. However, since we need the boundedness of the derivatives of the far field operator up to the second order, the shape needs to be more regular, see [15] for the formulation of the second domain derivative of the far field operator. In this case, the far field operator can be proved to be twice continuously differentiable with respect to r and k.*

In the following sections, we denote by $u_m^{\infty,\delta}(\cdot,k)$ the noisy measured far field pattern, which is assumed to belong to $L^2(\mathbb{S}^1)$, at the wavenumber k with the noise level $\delta \geq 0$. We define the operator $\tilde{F}_\delta$ from X^+ to Y by $\tilde{F}_\delta(r,k) := F(r,k) - u_m^{\infty,\delta}(\cdot,k)$. Using the recursive optimization methods, we determine the obstacle's shape by minimizing the objective functional

$$G_\delta(r,k) := \frac{1}{2} \|\tilde{F}_\delta(r,k)\|_Y^2, r \in X^+, \tag{9}$$

recursively with respect to frequency. That is, we first minimize $G_\delta(r,k_l)$ at the lowest frequency k_l. Then the obtained solution is used as an initial guess to minimize the objective functional (9) at a higher frequency. The process is repeated until the highest frequency.

3 Obstacle reconstruction at the lowest frequency

To minimize the objective functional $G_\delta(r, k_l)$, we make use of gradient-based iterative algorithms. Since these algorithms can, in general, only determine a local minimum of $G_\delta(r, k_l)$, it is necessary to start from a "good" initial guess. To quantify how good the initial guess should be, we derive a quantitative result concerning the set of local convexity of $G_\delta(r, k_l)$. We show in the following that this set is inversely proportional to the wavenumber k_l. As a consequence, for k_l high, the objective functional is very oscillatory and has many local minima which needs an initial guess close to the true solution. On the contrary, for small k_l, the set of local convexity around its solution is large enough which allows us to obtain an approximation of the true solution without the need of a good initial guess.

We should note that the results of this section are not only crucial for the performance of the RLA but also of importance on their own in the framework of inverse scattering theory. In particular, it shows how a quantitative uniqueness result of the inverse problem provides an estimate of the set of local convexity of the corresponding objective functional to be minimized.

Denote by r_e the radial function of the true shape. Let us first consider the noiseless data, i.e., $\delta = 0$. Recall that $\tilde{F}_0(r_e, k_l) = 0$. The following theorem gives an explicit estimate of the region of local convexity of the objective functional $G_0(\cdot, k_l)$.

Theorem 3.1. *Suppose that the obstacle D is contained in the disk $B(x^0, \frac{\pi}{k_l})$ centered at the point x^0 as given in (5) and radius $\frac{\pi}{k_l}$. Then the objective functional $G_0(\cdot, k_l)$ is convex in the set $B(\frac{\pi}{k_l}) := \{r \in X^+ : \|r\| \leq \frac{\pi}{k_l}\}$, where $\|r\|$ represents the maximum norm of r.*

Proof. The proof is based on the quantitative uniqueness result of Colton and Sleemann [11] and the injectivity of the domain derivative $\partial_r F(r, k_l)$. Recall the definition of the derivative of $G_0(\cdot, k_l)$ at r in the direction $a \in X$:

$$G_0'(r, k_l)a := \lim_{\epsilon \searrow 0} \frac{G_0(r + \epsilon a, k_l) - G_0(r, k_l)}{\epsilon}.$$

From (9) we have

$$\begin{aligned} G_0'(r, k_l)a &= \frac{1}{2} \lim_{\epsilon \searrow 0} \int_{\mathbb{S}^1} \frac{\tilde{F}_0^2(r + \epsilon a, k_l) - \tilde{F}_0^2(r, k_l)}{\epsilon} \mathrm{d}s \\ &= \int_{\mathbb{S}^1} \tilde{F}_0(r, k_l) \partial_r \tilde{F}_0(r, k_l) a \mathrm{d}s. \end{aligned} \tag{10}$$

Suppose that $r \in X^+$ is an extreme point of $G_0(\cdot, k_l)$. Then we have $G_0'(r, k_l)a = 0$ for all $a \in X$. On the other hand, it follows from Lemma 2.2 that the domain derivative $\partial_r \tilde{F}_0(r, k_l)$, which is equal to $\partial_r F(r, k_l)$, is injective. Moreover, as remarked by Kress [21], this operator can be extended to be a bounded linear operator, which we also denote by $\partial_r \tilde{F}_0(r, k_l)$, from $L^2[0, 2\pi]$ to $L^2(\mathbb{S}^1)$ and this extended operator has a dense range. From the denseness of X in $L^2[0, 2\pi]$

we deduce that the set $\{\partial_r \tilde{F}_0(r,k_l)a,\ a \in X\}$ is dense in $L^2(\mathbb{S}^1)$. Therefore, it follows from (10) that $\tilde{F}_0(r,k_l) \equiv 0$. This is equivalent to $G_0(r,k_l) = 0$.

Now we make use of the uniqueness result by Colton and Sleeman [11]. It says that, using one incident plane wave, the inverse obstacle problem has a unique solution provided that the obstacle falls within the disk centered at the origin and radius $\frac{\pi}{k_l}$. It is still true for the disk of the same radius centered at x^0. This uniqueness implies that r_e is the only zero point of the objective functional $G_0(\cdot,k_l)$ in $B(\frac{\pi}{k_l})$. Thus, $G_0(\cdot,k_l)$ has only one extreme point in the set $B(\frac{\pi}{k_l})$. Moreover, this point is a minimum of $G_0(\cdot,k_l)$. Hence, it is convex in $B(\frac{\pi}{k_l})$. The proof is complete. □

Next, let us consider the noisy operator $\tilde{F}_\delta(r,k_l)$ and the corresponding least-squares objective functional $G_\delta(r,k_l)$. We rewrite $\tilde{F}_\delta$ as

$$\tilde{F}_\delta(r,k_l) = \tilde{F}_0(r,k_l) + f^\delta(r_e,k_l),$$

where $f^\delta(r_e,k_l) := F(r_e,k_l) - u_m^{\infty,\delta}(\cdot,k_l)$ represents the noisy term with $\|f^\delta(r_e,k_l)\|_Y \le \delta$. Due to the presence of the noise, the objective functional $G_\delta(\cdot,k_l)$ may not be convex in the set $B(\frac{\pi}{k_l})$ any more. To restore its convexity, we add a Tikhonov regularization term, i.e., we consider the following regularized objective functional

$$G_\gamma(r,k_l) = \frac{1}{2}\|\tilde{F}_0(r,k_l) + f^\delta(r_e,k_l)\|_Y^2 + \frac{1}{2}\gamma\|r\|_X^2, r \in X^+, \tag{11}$$

where γ is a positive parameter known as the regularization parameter. We show that for properly chosen γ, the objective functional $G_\gamma(\cdot,k_l)$ becomes convex in the set $B(\frac{\pi}{k_l})$. Indeed, differentiating (11) with respect to r twice, we obtain:

$$\begin{aligned} G_\gamma''(r,k_l)(a,a) &= \Big(\tilde{F}_0(r,k_l) + f^\delta(r_e,k_l), \partial_{rr}^2\tilde{F}_0(r,k_l)(a,a)\Big)_Y + \|\partial_r\tilde{F}_0(r,k_l)a\|_Y^2 + \gamma\|a\|_X^2 \\ &= G_0''(r,k_l)(a,a) + \Big(f^\delta(r_e,k_l), \partial_{rr}^2\tilde{F}_0(r,k_l)(a,a)\Big)_Y + \gamma\|a\|_X^2,\ \forall a \in X. \end{aligned}$$

Since the noiseless objective functional $G_0(\cdot,k_l)$ is convex in $B(\frac{\pi}{k_l})$, $G_0''(r,k_l)(a,a) \ge 0\ \forall r \in B(\frac{\pi}{k_l}), \forall a \in X$. If γ is chosen to be $\gamma = d\delta$ with $d \ge \max\limits_{r\in B(\frac{\pi}{k_l})} \|\partial_{rr}^2\tilde{F}_0(r,k_l)\|_{\mathcal{L}(X\times X,Y)}$, which is bounded (see Remark 2.1), then it is clear that $G_\gamma''(r,k_l)$ is positive semi-definite in $B(\frac{\pi}{k_l})$. As a consequence, $G_\gamma(\cdot,k_l)$ is also convex in the same set.

We summarize the above analysis in the following theorem.

Theorem 3.2. *Let $\delta \ge 0$ be the measured noise level. Then with the regularization parameter γ chosen to be $\gamma = d\delta$, $d \ge \max\limits_{r\in B(\frac{\pi}{k_l})} \|\partial_{rr}^2\tilde{F}_0(r,k_l)\|_{\mathcal{L}(X\times X,Y)}$, the regularized objective functional $G_\gamma(\cdot,k_l)$ is convex in the set $B(\frac{\pi}{k_l})$.*

From this theorem we can conclude that, any radial function in the set $B(\frac{\pi}{k_l})$ can be used as an initial guess for locally convergent gradient-based methods to obtain an approximation

of the exact shape. Clearly, the smaller k_l, the larger the set. In particular, if the obstacle is expected to fall into a given region, we should start with k_l small enough so that $B(\frac{\pi}{k_l})$ contains this region. Note that the radius of the convex disk in Theorems 3.1 and 3.2 can also be chosen to be $\frac{4.49}{k_l}$ based on the uniqueness result by Gintides [13] which improved the result of Colton and Sleeman. We can also use the local uniqueness result of Stefanov and Uhlmann [26] to prove the local convexity of the objective functionals $G_0(\cdot, k_l)$ and $G_\gamma(\cdot, k_l)$ at an arbitrary frequency.

4 Recursive linearization algorithm and its convergence rate

The reconstruction at the lowest frequency k_l provides an approximation of the obstacle. However, due to the poor stability of the reconstruction problem at low frequencies, the result of this step is just a rough estimate of the obstacle. To enhance the reconstruction accuracy, we make use of the RLA, as an example of the recursive optimization methods, to obtain approximations at higher frequencies. The algorithm was first described in [7] for medium scattering problems. The idea of this algorithm is to replace the original nonlinear ill-posed problem at each frequency by a linearized one. The linearization is done using Taylor expansion of the far field operator at a solution of the inverse problem at a lower frequency. The algorithm is described hereafter for the problem under consideration.

4.1 Description of the RLA

Suppose that the far field pattern is measured at the discrete set of frequencies $k_j := k_l + j\Delta k, j = 0, 1, \ldots, N$, with $\Delta k = \frac{k_h - k_l}{N}$. Assume further that we have a rough approximation r_0 of the exact radial function at the lowest frequency $k_0 = k_l$, which can be obtained by the first step described in the previous section. At the wavenumber k_{j+1}, given an approximation r_j at k_j, we write the far field operator F as

$$F(r, k_{j+1}) = F(r_j, k_{j+1}) + \partial_r F(r_j, k_{j+1})(r - r_j) + O(\|r - r_j\|_X^2).$$

The nonlinear objective functional $G_\delta(r, k_{j+1})$ given by (9) is linearized using this equality. Then, we find an approximation r_{j+1} at k_{j+1} by $r_{j+1} = r_j + \Delta r_j$, with Δr_j being the solution to the linear least-squares problem

$$\Delta r_j := \text{argmin}_{\Delta r} \frac{1}{2} \|\tilde{F}_\delta(r_j, k_{j+1}) + \partial_r F(r_j, k_{j+1})\Delta r\|_Y^2.$$

Since this problem is generally ill-posed, we replace it by the following regularized one using the Tikhonov regularization method

$$\Delta r_j := \text{argmin}_{\Delta r} \left\{ \frac{1}{2} \|\tilde{F}_\delta(r_j, k_{j+1}) + \partial_r F(r_j, k_{j+1})\Delta r\|_Y^2 + \frac{1}{2}\alpha \|\Delta r\|_X^2 \right\}. \tag{12}$$

The solution to this minimization problem is given by

$$\Delta r_j = -(\alpha I + A_j^* A_j)^{-1} A_j^* \tilde{F}_\delta(r_j, k_{j+1}),$$

where $A_j = \partial_r F(r_j, k_{j+1})$ and A_j^* is its adjoint operator. Hence, the approximation r_{j+1} is given by

$$r_{j+1} = r_j - (\alpha I + A_j^* A_j)^{-1} A_j^* \tilde{F}_\delta(r_j, k_{j+1}). \tag{13}$$

The equation (13) is solved recursively until the highest wavenumber $k_N = k_h$. The algorithm is summarized as follows.

Algorithm 4.1 (Recursive linearization algorithm)**.**

- *Given $u_m^{\infty,\delta}(\cdot, k)$ for $k = k_0, \ldots, k_N$ and the parameters $\alpha > 0$, $\gamma > 0$.*
- *Step 1: find an approximation r_0 of r at the lowest frequency k_0 by minimizing the objective functional* (11)*.*
- *Step 2 (recurrence)*

  For $j = 0, \ldots, N-1$

  - *Calculate $\tilde{F}_\delta(r_j, k_{j+1}) = F(r_j, k_{j+1}) - u_m^{\infty,\delta}(\cdot, k_{j+1})$.*
  - *Calculate $A_j = \partial_r F(r_j, k_{j+1})$ and its adjoint A_j^*.*
  - *Update the reconstruction: $r_{j+1} = r_j - (\alpha I + A_j^* A_j)^{-1} A_j^* \tilde{F}_\delta(r_j, k_{j+1})$.*

  End (for).

The approximation r_N is considered as the reconstruction result of the RLA. The convergence of the algorithm is discussed in the next subsection, while its accuracy is investigated in Section 5.

To implement Algorithm 4.1, it is necessary to represent the radial functions r_j as functions of a finite number of parameters. Since any radial function $r(t)$ satisfies $r(0) = r(2\pi)$, it can be considered as a periodic function with the period of 2π. Hence, we can represent it as the following Fourier series

$$r(t) = \beta_0 + \sum_{m=1}^{\infty} (\beta_m \cos mt + \gamma_m \sin mt). \tag{14}$$

We note that the Fourier coefficients β_m and γ_m converge to zero at infinity. Their convergence rate depends on the smoothness of the function $r(t)$, see [12]. For each number $M \in N$, we define the cut-off approximation $r^M(t)$ of $r(t)$ by

$$r^M(t) := \beta_0 + \sum_{m=1}^{M} (\beta_m \cos mt + \gamma_m \sin mt). \tag{15}$$

It is clear that, for large M, r^M is different from r just in high frequency modes which represent small details of the obstacle shape. For a given value $\tilde{\delta} > \delta$, there exists a number $M_0(k) \in N$ depending on k such that $\|F(r^M, k) - F(r, k)\|_Y \leq \tilde{\delta} - \delta$ for all $M \geq M_0(k)$. Consequently, $\|F(r^M, k) - u_m^{\infty,\delta}(\cdot, k)\|_Y \leq \tilde{\delta}$ for $M \geq M_0(k)$. Note that $M_0(k)$ depends also on $\tilde{\delta}$ and δ, but

we ignore these parameters since they are fixed throughout the rest of this section. From this analysis, we can simplify the inverse problem by determining the cut-off approximation r^M (or its Fourier coefficients) instead of the radial function r itself. By this simplification, the inverse problem becomes finite dimensional. For later use, we denote by X_M the subspace of X which contains all functions of the form (15), i.e., X_M is spanned by $\{1, \cos t, \sin t, \ldots, \cos Mt, \sin Mt\}$ and $X_M^+ := \{\varphi \in X_M : \varphi(t) > 0, \forall t \in [0, 2\pi]\}$. In the following, we focus on reconstructing a *finite dimensional observable shape* which is defined as follows.

Definition 4.2. *For each wavenumber k and a given $\tilde{\delta} > \delta$, a finite dimensional observable shape (or, in short, observable shape) $D(\tilde{r}(k))$ is defined as a domain of which the radial function $\tilde{r}(k) \in X_M^+$ for some $M \in \mathbb{N}$ and the corresponding far field pattern $F(\tilde{r}(k), k)$ satisfies the condition $\|F(\tilde{r}(k), k) - u_m^{\infty,\delta}(\cdot, k)\|_Y \leq \tilde{\delta}$.*

It is obvious that $D(r^M)$ is a finite dimensional observable shape of the obstacle $D(r)$ for $M \geq M_0(k)$. However, we should emphasize that, there may be several finite dimensional observable shapes which are very different from $D(r^M)$ due to the ill-posedness of the considered inverse problem. The question on how these observable shapes approximate the original one relates closely to the stability of the inverse problem. This topic is discussed in Section 5.

Remark 4.1. *In the above definition, we made use of the value $\tilde{\delta}$ instead of the noise level δ because if the latter is used, the finite dimensional observable shapes may not exist. However, it is possible to choose $\tilde{\delta}$ close to δ while $M_0(k)$ can still be chosen not too large. This can be explained using the Heisenberg's uncertainty principle in Physics on the resolution limit of scattering problems. It says that, at a fix frequency, we cannot observe small details of the scatterer using noisy measurements of the far field pattern, regardless the noise magnitude. In other words, choosing too many Fourier modes does not help to improve the reconstruction accuracy but increases the instability of the reconstruction. Therefore, $M_0(k)$ should not be chosen too large. As shown in [7], this resolution limit is about half of the wavelength for weak scatterers, see also [3, 4]. Due to this uncertainty principle, we also choose r_j, $j = 0, \ldots, N$, in Algorithm 4.1 such that they contain finite numbers of Fourier modes.*

4.2 Convergence of the RLA

To prove the convergence of the RLA, the following lemma on compact operators is needed. It can be proved using the spectral theory of linear operators.

Lemma 4.3. *Let A be a compact linear operator from a Banach space X to a Banach space Y and $R_\alpha(A) := (\alpha I + A^*A)^{-1}A^*$ with $\alpha > 0$. Then*

$$\|(\alpha I + A^*A)^{-1}\|_{\mathcal{L}(X,Y)} \leq \frac{1}{\alpha}, \tag{16}$$

$$\|R_\alpha(A)\|_{\mathcal{L}(Y,X)} \leq \frac{1}{2\sqrt{\alpha}}, \tag{17}$$

$$\|R_\alpha(A)A\|_{\mathcal{L}(X,X)} \leq 1. \tag{18}$$

Moreover, if $\tilde{A}$ is also a compact linear operator from X to Y, we have

$$\|R_\alpha(A) - R_\alpha(\tilde{A})\|_{\mathcal{L}(Y,X)} \leq \frac{9}{4\alpha}\|A - \tilde{A}\|_{\mathcal{L}(X,Y)}. \tag{19}$$

For the proof of convergence of the RLA, we make use of **the assumption** that there exists a constant $d_0 > 0$ such that the set $\{\tilde{r}(k_j), j = 0, \ldots, N\}$ of the radial functions of the observable shapes satisfies

$$\|\tilde{r}(k_{j+1}) - \tilde{r}(k_j)\|_X \leq d_0|k_{j+1} - k_j|, \forall j = 0, \ldots, N-1. \tag{20}$$

Remark 4.2. *Concerning the existence of this set of observable shapes, we can choose $\tilde{r}(k_j) = r^M$ $\forall j = 0, \ldots, N$, with $M \geq M_0(k_h)$ fixed. For this fixed observable shape, the convergence of the RLA is guaranteed if $\tilde{\delta} = 0$. However, in the case of noisy data, the assumptions of Theorem 4.5 may not be satisfied for this choice of the observable shapes. In this case, the number of Fourier modes of $\tilde{r}(k)$ must be chosen to be increasing as k increases, see condition* (45) *below and Remark 4.3. A rigorous proof for the existence of the radial functions $\tilde{r}(k_j), j = 0, \ldots, N$, satisfying both* (20) *and the hypothesis of Theorem 4.5 is still missed in general.*

However, if the exact domain is smooth enough, say, of class C^5, and the weak scattering is valid, we can point out a set of truncated Fourier expansions of r which satisfies this assumption. Indeed, consider two truncated functions $r^{M(k_1)}$ and $r^{M(k_2)}$ of the form (15) *with $M(k_1) \leq M(k_2)$ which correspond to two observable shapes at k_1 and k_2, respectively. It is clear that*

$$r^{M(k_2)}(t) - r^{M(k_1)}(t) = \sum_{m=M(k_1)+1}^{M(k_2)} (\beta_m \cos mt + \gamma_m \sin mt).$$

Since $r \in C^5[0, 2\pi]$, the Fourier coefficients β_m and γ_m satisfy $\beta_m = o(\frac{1}{m^5})$ and $\gamma_m = o(\frac{1}{m^5})$, see [12]. Note that we only need to deal with the third derivative, the other terms are similar and easier. Differentiating both sides three times and taking the $C-$norm, we have

$$\begin{aligned}\|\frac{d^3\left[r^{M(k_2)} - r^{M(k_1)}\right]}{dt^3}\|_C &= \|\sum_{m=M(k_1)+1}^{M(k_2)} m^3(\beta_m \sin mt \gamma_m \cos mt)\|_C \\ &\leq 2\sum_{m=M(k_1)+1}^{M(k_2)} \frac{1}{m^2} \leq 2\frac{M(k_2) - M(k_1)}{M(k_1)M(k_2)}.\end{aligned}$$

Using the Heisenberg's uncertainty principle, it was shown in [7] that in case of weak scattering, it is only possible to stably reconstruct the Fourier modes up to approximately $2k$. That is, $M(k_j)$ can be chosen to be $\approx 2k_j$. Replacing this into the above equation, we obtain (20).

For the radial functions $\tilde{r}(k), k \in [k_l, k_h]$ associated with a given set of finite dimensional observable shapes of r, we write the operator $\tilde{F}_\delta$ as

$$\tilde{F}_\delta(r, k) = \tilde{F}(r, k) + f^{\tilde{\delta}}(\tilde{r}(k), k) \tag{21}$$

with $\tilde{F}(r,k) := F(r,k) - F(\tilde{r}(k),k)$ and $f^{\tilde{\delta}}(\tilde{r}(k),k) := F(\tilde{r}(k),k) - u_m^{\infty,\delta}(\cdot,k)$. Note that $\|f^{\tilde{\delta}}(\tilde{r}(k),k)\|_Y \leq \tilde{\delta}$. It is obvious that

$$\tilde{F}(\tilde{r}(k),k) = 0, \forall k \in [k_l, k_h]. \tag{22}$$

It follows from Remark 2.1 that $\tilde{F}(r,k)$ is twice continuously differentiable. That is, there exist some positive constants $d_i, i = 1,\ldots,5$, such that for all $r \in B(\frac{\pi}{k_l})$ and $k \in [k_l, k_h]$, we have

$$\begin{aligned} &\|\partial_r \tilde{F}(r,k)\|_{\mathcal{L}(X,Y)} \leq d_1,\ \|\partial_k \tilde{F}(r,k)\|_Y \leq d_2, \\ &\|\partial^2_{rr} \tilde{F}(r,k)\|_{\mathcal{L}(X\times X,Y)} \leq d_3,\ \|\partial^2_{rk} \tilde{F}(r,k)\|_{\mathcal{L}(X,Y)} \leq d_4,\ \|\partial^2_{kk} \tilde{F}(r,k)\|_Y \leq d_5. \end{aligned} \tag{23}$$

The following lemma shows the convergence rate of the RLA for the noiseless data. We note that this lemma was proved by Bao and Triki in [4] for a general setup. However, since some arguments of its proof are needed for the case of noisy data, we repeat it here for the convenience of the reader. Moreover, we should remark that in this lemma, the assumption **H2** in [4] on the twice differentiability of the observable shape $\tilde{r}(k)$ with respect to k is replaced by the weaker condition (20) and the assumption **H3** in [4] is not needed. We also simplify their proof.

Lemma 4.4. *Assume that the observable shapes $\tilde{r}(k_j), j = 0,\ldots,N$, satisfy the condition* (20) *and $r_j, j = 0,\ldots,N$, are given by Algorithm 4.1 with $\tilde{F}_\delta$ being replaced by $\tilde{F}$. Then there exist constants α, c_0 and N_0 such that if*

$$\|\tilde{r}(k_l) - r_0\|_X \leq c_0\alpha, \tag{24}$$

then the following error estimate holds

$$\|\tilde{r}(k_h) - r_N\|_X \leq \frac{C}{N\sqrt{\alpha}}, \forall N \geq N_0, \tag{25}$$

where C is a constant independent of α and N.

Proof. Denote by $e_j := \tilde{r}(k_j) - r_j$, $R_j := (\alpha I + A_j^* A_j)^{-1} A_j^*$ and $\tilde{R}_j := (\alpha I + \tilde{A}_j^* \tilde{A}_j)^{-1} \tilde{A}_j^*$, where $\tilde{A}_j := \partial_r F(\tilde{r}(k_j), k_j)$. It follows from (13) and (21) that

$$\begin{aligned} e_{j+1} =& \tilde{r}(k_{j+1}) - r_j + R_j \tilde{F}(r_j, k_{j+1}) \\ =& \tilde{r}(k_{j+1}) - \tilde{r}(k_j) + e_j - \tilde{R}_j \tilde{A}_j e_j + \tilde{R}_j \tilde{A}_j e_j + R_j \tilde{F}(r_j, k_{j+1}). \end{aligned} \tag{26}$$

Let us evaluate the right hand side. Firstly, the first two terms are estimated by (20). Secondly, since both $\tilde{r}(k_j)$ and r_j have finite numbers of Fourier modes, see Remark 4.1, there exists a finite dimensional subspace X_{M_j} of X which contains both of them. Therefore, as $\tilde{A}_j$ is injective by Lemma 2.2, the smallest singular value σ_j of this operator restricted to X_{M_j}, $\tilde{A}_j\big|_{X_{M_j}}$, is positive. We denote by $\sigma := \min\{\sigma_j, \ldots, \sigma_N\}$. It is obvious that $\sigma > 0$. The spectral theory implies that

$$\|e_j - \tilde{R}_j \tilde{A}_j e_j\|_X \leq \frac{\alpha}{\alpha + \sigma^2} \|e_j\|_X. \tag{27}$$

Thirdly,

$$\begin{aligned}\tilde{R}_j\tilde{A}_j e_j + R_j\tilde{F}(r_j,k_{j+1}) = \tilde{R}_j[\tilde{A}_j e_j + \tilde{F}(r_j,k_j)] - (\tilde{R}_j - R_j)\tilde{F}(r_j,k_j)\\ + R_j[\tilde{F}(r_j,k_{j+1}) - \tilde{F}(r_j,k_j)].\end{aligned} \tag{28}$$

Using the Taylor expansion of $\tilde{F}(r_j,k_j)$ at $\tilde{r}(k_j)$ up to the second order, (17) and (22)–(23), we have

$$\|\tilde{R}_j[\tilde{A}_j e_j + \tilde{F}(r_j,k_j)]\|_X \le \frac{d_3}{4\sqrt{\alpha}}\|e_j\|_X^2. \tag{29}$$

On the other hand, it follows from Lemma 4.3 and (22)–(23) that

$$\begin{aligned}\|(\tilde{R}_j - R_j)\tilde{F}(r_j,k_j)\|_X &\le \frac{9}{4\alpha}\|A_j - \tilde{A}_j\|_{\mathcal{L}(X,Y)}\|\tilde{F}(r_j,k_j) - \tilde{F}(\tilde{r}(k_j),k_j)\|_Y\\ &\le \frac{9d_1}{4\alpha}\|A_j - \tilde{A}_j\|_{\mathcal{L}(X,Y)}\|e_j\|_X.\end{aligned}$$

From the definition of A_j and $\tilde{A}_j$ we have

$$\begin{aligned}\|A_j - \tilde{A}_j\|_{\mathcal{L}(X,Y)} \le& \|\partial_r\tilde{F}(r_j,k_{j+1}) - \partial_r\tilde{F}(r_j,k_j)\|_{\mathcal{L}(X,Y)}\\ &+ \|\partial_r\tilde{F}(r_j,k_j) - \partial_r\tilde{F}(\tilde{r}(k_j),k_j)\|_{\mathcal{L}(X,Y)}\\ \le& \Delta k d_4 + d_3\|e_j\|_X.\end{aligned}$$

Replacing this estimate into the above inequality we obtain

$$\|(\tilde{R}_j - R_j)\tilde{F}(r_j,k_j)\|_X \le \frac{9d_1}{4\alpha}\left[\Delta k d_4 + d_3\|e_j\|_X\right]\|e_j\|_X. \tag{30}$$

It follows from (23) that

$$\|R_j[\tilde{F}(r_j,k_{j+1}) - \tilde{F}(r_j,k_j)]\|_X \le \frac{d_2}{2\sqrt{\alpha}}\Delta k. \tag{31}$$

Substituting (29)–(31) into (28), we obtain

$$\|\tilde{R}_j\tilde{A}_j e_j + R_j\tilde{F}(r_j,k_{j+1})\|_X \le \frac{d_2}{2\sqrt{\alpha}}\Delta k + \left(\frac{9d_1d_3}{4\alpha} + \frac{d_3}{4\sqrt{\alpha}}\right)\|e_j\|_X^2. \tag{32}$$

By combining (20), (27) and (32) we have

$$\begin{aligned}\|e_{j+1}\|_X \le \Delta k\left(d_0 + \frac{d_2}{2\sqrt{\alpha}}\right) + \frac{\alpha}{\alpha+\sigma^2}\|e_j\|_X\\ + \frac{9d_1d_4}{4\alpha}\Delta k\|e_j\|_X + \left(\frac{9d_1d_3}{4\alpha} + \frac{d_3}{4\sqrt{\alpha}}\right)\|e_j\|_X^2.\end{aligned} \tag{33}$$

For a fixed value $\epsilon \in (0,1)$, we first choose α such that

$$\frac{\alpha}{\alpha+\sigma^2} \le \frac{\epsilon}{3} \tag{34}$$

which is equivalent to $\alpha \le \frac{\epsilon\sigma^2}{3-\epsilon}$. Next, the condition

$$\left(\frac{9d_1d_3}{4\alpha} + \frac{d_3}{4\sqrt{\alpha}}\right)\|e_j\|_X = \left(\frac{9d_1d_3}{4} + \frac{d_3}{4}\sqrt{\alpha}\right)\frac{\|e_j\|_X}{\alpha} \le \frac{\epsilon}{3} \tag{35}$$

is satisfied if $\|e_j\|_X \leq c_0\alpha$ with

$$c_0 := \frac{\epsilon}{3}\left(\frac{9d_1d_3}{4} + \frac{d_3}{4}\frac{\sqrt{\epsilon}\sigma}{\sqrt{3-\epsilon}}\right)^{-1}. \tag{36}$$

For the given α, we can also choose a number $N_1 = N_1(\alpha)$ such that for all $N \geq N_1$, we have

$$\frac{9d_1d_4}{4\alpha}\Delta k \leq \frac{\epsilon}{3} \tag{37}$$

(we recall that $\Delta k = \frac{k_h - k_l}{N}$) and

$$\Delta k\left(d_0 + \frac{d_2}{2\sqrt{\alpha}}\right) \leq (1-\epsilon)c_0\alpha. \tag{38}$$

It follows from (33)–(38) that $\|e_{j+1}\|_X \leq (1-\epsilon)c_0\alpha + \epsilon\|e_j\|_X$. Therefore, if $\|e_0\|_X \leq c_0\alpha$, we can prove by recurrence that $\|e_j\|_X \leq c_0\alpha$ for $j = 1, \ldots, N$. Hence,

$$\|e_{j+1}\|_X \leq \Delta k\left(d_0 + \frac{d_2}{2\sqrt{\alpha}}\right) + \epsilon\|e_j\|_X, \forall j = 0, \ldots, N-1.$$

Consequently,

$$\begin{aligned}\|e_N\|_X &\leq \Delta k\left(d_0 + \frac{d_2}{2\sqrt{\alpha}}\right)\frac{1-\epsilon^N}{1-\epsilon} + \epsilon^N\|e_0\|_X \\ &= \frac{k_h - k_l}{N\sqrt{\alpha}}\left\{\left(d_0\sqrt{\alpha} + \frac{d_2}{2}\right)\frac{1-\epsilon^N}{1-\epsilon} + \frac{\sqrt{\alpha}N\epsilon^N}{k_h - k_l}\|e_0\|_X\right\}.\end{aligned} \tag{39}$$

Since $N\epsilon^N$ is bounded in terms of N, there exists a constant $C > 0$ independent of N and α such that

$$(k_h - k_l)\left\{\left(d_0\frac{\sqrt{\epsilon}\sigma}{\sqrt{3-\epsilon}} + \frac{d_2}{2}\right)\frac{1-\epsilon^N}{1-\epsilon} + \frac{\sqrt{\epsilon}\sigma}{\sqrt{3-\epsilon}}\frac{N\epsilon^N}{k_h - k_l}\|e_0\|_X\right\} \leq C.$$

Replacing this inequality into (39) we obtain (25). The lemma is proved. □

Let us now consider the noisy operator $\tilde{F}_\delta$. In this case, the error is given by

$$e_{j+1} = \tilde{r}(k_{j+1}) - \tilde{r}(k_j) + e_j - \tilde{R}_j\tilde{A}_je_j + \tilde{R}_j\tilde{A}_je_j + R_j\tilde{F}(r_j, k_{j+1}) + R_jf^{\tilde{\delta}}(\tilde{r}(k_{j+1}), k_{j+1}). \tag{40}$$

It follows from Lemma 4.4 that

$$\|R_jf^{\tilde{\delta}}(\tilde{r}(k_{j+1}), k_{j+1})\|_X \leq \frac{\tilde{\delta}}{2\sqrt{\alpha}}. \tag{41}$$

Using the estimate (33) for the noiseless case, from (40)–(41) we have

$$\begin{aligned}\|e_{j+1}\|_X \leq{}& \Delta k\left(d_0 + \frac{d_2}{2\sqrt{\alpha}}\right) + \frac{\tilde{\delta}}{2\sqrt{\alpha}} + \frac{\alpha}{\alpha+\sigma^2}\|e_j\|_X \\ &+ \frac{9d_1d_4}{4\alpha}\Delta k\|e_j\|_X + \left(\frac{9d_1d_3}{4\alpha} + \frac{d_3}{4\sqrt{\alpha}}\right)\|e_j\|_X^2.\end{aligned} \tag{42}$$

For α satisfying the condition (34) and c_0 given by (36), we choose N_1 such that the condition (37) is satisfied and

$$\Delta k \left(d_0 + \frac{d_2}{2\sqrt{\alpha}} \right) \leq (1-\xi)(1-\epsilon)c_0\alpha, \tag{43}$$

where $\xi \in (0,1)$ is fixed. Furthermore, we assume that α is chosen such that

$$\frac{\tilde{\delta}}{2\sqrt{\alpha}} \leq \xi(1-\epsilon)c_0\alpha. \tag{44}$$

Or, equivalently,

$$\alpha^{3/2} \geq \frac{3\tilde{\delta}}{2\xi(1-\epsilon)\epsilon} \left(\frac{9d_1d_3}{4} + \frac{d_3}{4}\frac{\sqrt{\epsilon}\sigma}{\sqrt{3-\epsilon}} \right).$$

We note that the regularization parameter must also satisfy the inequality $\alpha \leq \frac{\epsilon\sigma^2}{3-\epsilon}$. Therefore, for the existence of α, the following condition must be satisfied

$$\left(\frac{\epsilon}{3-\epsilon} \right)^{3/2} \sigma^3 - \frac{3\tilde{\delta}}{2\xi(1-\epsilon)\epsilon} \left(\frac{9d_1d_3}{4} + \frac{d_3}{4}\frac{\sqrt{\epsilon}\sigma}{\sqrt{3-\epsilon}} \right) \geq 0. \tag{45}$$

This inequality can be rewritten as

$$\tilde{\delta} \leq \frac{\sigma^3}{a\sigma + b}, \tag{46}$$

with a and b being positive constants independent of σ and $\tilde{\delta}$ which can be calculated from (45). In this case, the regularization parameter α must be chosen so that

$$\left(\frac{\epsilon}{3-\epsilon} \right)^{3/2} \sigma^3 \geq \alpha^{3/2} \geq \frac{3\tilde{\delta}}{2\xi(1-\epsilon)\epsilon} \left(\frac{9d_1d_3}{4} + \frac{d_3}{4}\frac{\sqrt{\epsilon}\sigma}{\sqrt{3-\epsilon}} \right). \tag{47}$$

Under condition (47), using the same arguments as above, we obtain the following error estimate

$$\|e_N\|_X \leq \frac{C}{N\sqrt{\alpha}} + \frac{\tilde{\delta}}{2\sqrt{\alpha}(1-\epsilon)}$$

if $\|e_0\|_X \leq c_0\alpha$. We summarize the above analysis in the following theorem.

Theorem 4.5. *Let δ be the noise level of the measured far field patterns and $\tilde{\delta} > \delta$. Let X_{M_j} the subspace of X containing both r_j and $\tilde{r}(k_j)$, the radial functions of the observable shapes as defined in Definition 4.2, $j = 0, \ldots, N$. We assume that the smallest singular value σ of the linear operators $\tilde{A}_j|_{X_{M_j}}, j \in \{0, \ldots, N\}$, satisfies the condition (45) and the regularization parameter α satisfies (47) for some fixed values $\epsilon, \xi \in (0,1)$. Then there exists a constant $N_0 = N_0(\alpha)$ such that if*

$$\|\tilde{r}(k_l) - r_0\|_X \leq c_0\alpha, \tag{48}$$

then the following estimate holds

$$\|\tilde{r}(k_h) - r_N\|_X \leq \frac{C}{N\sqrt{\alpha}} + \frac{\tilde{\delta}}{2\sqrt{\alpha}(1-\epsilon)}, \forall N \geq N_0, \tag{49}$$

where c_0 is given by (36) and C is a constant independent of $\tilde{\delta}$, α and N.

It is clear that the second term on the right hand side of (49) converges to zero as $\tilde{\delta}$ tends to zero due to the condition (47) (we note that it is not necessary to choose the regularization parameter α to converge to zero as the noise level tends to zero). That means, for $\tilde{\delta} = 0$ we obtain the noiseless error estimate as in Lemma 4.4. However, we emphasize that the noiseless assumption used in [4] is not applicable here even for exact far field measurements. The reason is that the finite dimensional observable shape is generally different from the exact one (except when the exact shape has a finite number of nonzero Fourier modes). Therefore, their far field patterns must be different due to the local uniqueness, see [26]. Moreover, the hypothesis **H3** and Lemma 3.2 of [4] are not enough to guarantee that the condition (45) is satisfied.

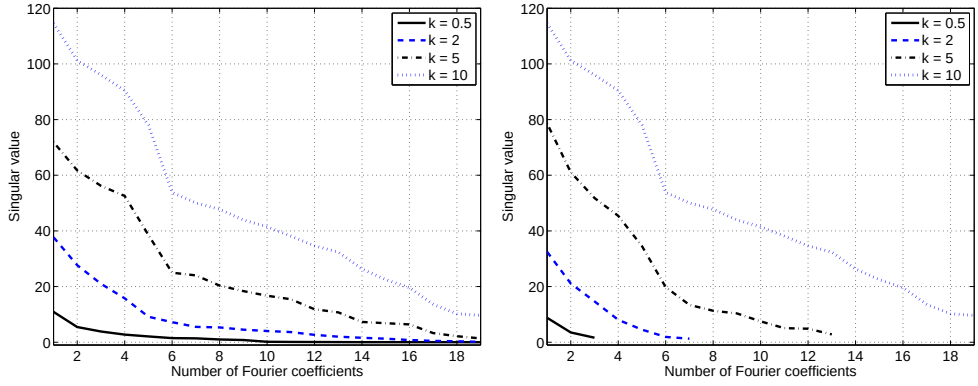

(a) (b)

Figure 1: Singular values of the operator $\tilde{A}_j$ associated with a flower-shaped obstacle: (a) for a fixed number of Fourier modes at all frequencies; (b) For increasing numbers of Fourier modes.

Remark 4.3. *Unlike the case of noiseless data, the smallest singular value σ must satisfy the condition* (45)*. It says that σ must be large enough compared to the noise level. The justification of this condition for an arbitrary obstacle and an arbitrary noise level is still open to us. However, this condition is satisfied for small enough noise level. Moreover, let us explain the link between this condition and the number of Fourier modes chosen in the reconstruction. For this purpose, we show in Figure 1 the singular values of the operators $\tilde{A}_j$ associated with a flower-shaped obstacle (see Section 6) at four wavenumbers of 0.5, 2, 5 and 10. In Figure 1(a), the observable shapes $\tilde{r}(k_j)$ are chosen the same as the true one at all frequencies which contains 19 Fourier coefficients while in Figure 1(b) the observable shapes contain respectively 3, 7, 11 and 19 Fourier coefficients.*

The figure indicates that, on the one hand, for a given sequence of frequencies, the more Fourier modes to be reconstructed, the smaller σ. Therefore, the higher the noise level is, the smaller the number of Fourier modes must be chosen. In other words, we should not try to reconstruct small details if the noise level is high.

On the other hand, for a given noise level, since the singular values of the operators $\tilde{A}_j$ increase when the frequency is increased, we should choose a small number of Fourier modes for

the lowest frequency and add more and more modes when we increase the frequency. Condition (45) *also suggests that we should increase the highest frequency to reconstruct more Fourier modes, or small details, of the obstacle.*

5 Stability of the inverse problem at high frequencies

The RLA reconstructs an approximation of the observable shape $D(\tilde{r}(k_h))$ of the obstacle at the highest frequency k_h. To complete the analysis, we need to investigate the link between the observable and the exact shapes or, in other words, the stability of the inverse problem at the highest frequency. To do so, let us analyze the behavior of the far field pattern at high frequencies. We note that the multifrequency data is not needed in this section. Instead, only one high frequency and one incident direction, but multiple observation directions, are required for the stability estimate. In this section, we only consider strictly convex obstacles.

The far field pattern of problem (1)–(3) with wavenumber k can be represented by the following integral form due to the Green's theorem [10]

$$u^\infty(\hat{x},\theta,k) = -\frac{e^{i\pi/4}}{\sqrt{8\pi k}} \int\limits_{\partial D} \frac{\partial u(y)}{\partial \nu(y)} e^{-ik\hat{x}\cdot y} \mathrm{d}s(y).$$

In the high frequency regime, the normal derivative $\frac{\partial u(y)}{\partial \nu(y)}$ of the total field can be approximated by (Kirchhoff approximation)

$$\frac{\partial u(y)}{\partial \nu(y)} = 2\frac{\partial u^i(y)}{\partial \nu(y)} \text{ for } y \in \partial D_+, \quad \frac{\partial u(y)}{\partial \nu(y)} = 0 \text{ for } y \in \partial D_-,$$

where ∂D_+ and ∂D_- are respectively the illuminated part and the shadowed part of the boundary ∂D by the incident wave defined as follows

$$\partial D_+ := \{x \in \partial D : \nu(x)\cdot\theta < 0\}, \quad \partial D_- := \{x \in \partial D : \nu(x)\cdot\theta \geq 0\}.$$

Thus the far field pattern can be rewritten as

$$u^\infty(\hat{x},\theta,k) = -\frac{ike^{i\pi/4}}{\sqrt{2\pi k}} \int\limits_{\partial D_+} \theta\cdot\nu(y) e^{ik(\theta-\hat{x})\cdot y} \mathrm{d}s(y). \tag{50}$$

From this equation we see that the far field pattern depends only on the illuminated part of the obstacle's boundary at high frequencies. Now let us represent (50) for the star-shaped obstacle using (5). Without loss of generality, we assume that ∂D_+ is given by

$$\partial D_+ = \{x(t) \in \mathbb{R}^2 : x(t) = r(t)(\cos t, \sin t), t \in (t_1, t_2)\},$$

with $t_1 < t_2$. Using this parametrization, we obtain

$$u^\infty(\hat{x},\theta,k) = -\frac{ike^{i\pi/4}}{\sqrt{2\pi k}} \int\limits_{t_1}^{t_2} \theta\cdot\nu(x(t))|x'(t)| e^{ik|\theta-\hat{x}|\varphi(t)} \mathrm{d}t, \tag{51}$$

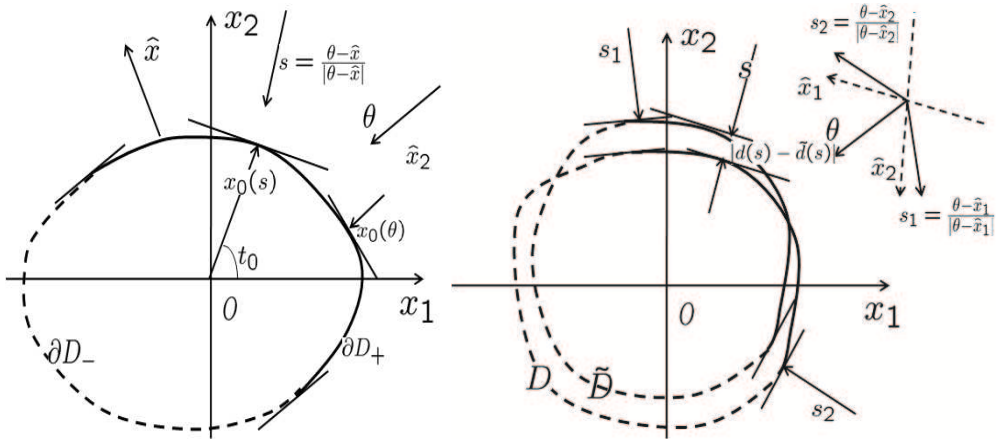

Figure 2: (a) Illustration of the illuminated part (the solid curve), the shadowed part (the dashed curve) and the specular points; (b) Relation between the support functions of two obstacles.

where $\varphi(t) := \frac{\theta-\hat{x}}{|\theta-\hat{x}|} \cdot (\cos t, \sin t) r(t)$. To approximate the integral of (51) in the high frequency regime, the stationary phase method can be used. Here, we follow the arguments of Gutman and Ramm [14] for reconstructing the so-called *support function* and the curvature of the obstacle. We define the *specular point* $x_0(s) \in \partial D_+$ associated with a vector $s \in \mathbb{S}^1$ from the condition $x_0(s) \cdot s = \min_{x \in \partial D_+} x \cdot s$, see Figure 2(a). The support function $d(s)$ is defined by

$$d(s) := x_0(s) \cdot s.$$

As noted in [14], $|d(s)|$ is the distance from the origin to the unique tangent line to ∂D_+ perpendicular to s. For the given direction of incidence θ and an observation direction $\hat{x} \neq \theta$, we denote by $t_0 \in (t_1, t_2)$ such that $x_0(s) := (\cos t_0, \sin t_0) r(t_0)$ is the specular point associated with the vector

$$s := \frac{\theta - \hat{x}}{|\theta - \hat{x}|}. \tag{52}$$

Note that, due to the strict convexity of D, there exists a one-to-one correspondence between $t_0 \in (t_1, t_2)$ and $\hat{x} \in \mathbb{S}^1 \setminus \{\theta\}$. Moreover, t_0 is the unique minimum point of $\varphi(t)$. Note that $\varphi(t_0) = d(s)$. Using the stationary phase method, see Theorem 7.7.5 of [17], we obtain

$$u^\infty(\hat{x}, \theta, k) = -\frac{1}{2}\sqrt{\frac{|\theta - \hat{x}|}{\kappa(x_0(s))}} e^{ik|\theta-\hat{x}|d(s)} \left[1 + O(\frac{1}{k|\theta - \hat{x}|})\right], \tag{53}$$

where $\kappa(x_0(s))$ is the curvature of the shape at $x_0(s)$ which is positive due to the strict convexity of D. Note that we replace the term $O(\frac{1}{k})$ in [14] by $O(\frac{1}{k|\theta-\hat{x}|})$ to take into account the effect of $|\theta - \hat{x}|$ on the validity of the expansion (53). From this equality, we obtain the following stability estimate for the curvature.

Theorem 5.1. *Let D and $\tilde{D}$ be two strictly convex sound-soft obstacles whose curvatures are bounded from below by $\kappa_l > 0$. For a given incident direction $\theta \in \mathbb{S}^1$ and an observation direction $\hat{x} \neq \theta$, we denote by $\kappa(x_0(s))$ and $\tilde{\kappa}(\tilde{x}_0(s))$ the curvature of D and $\tilde{D}$ at the specular points $x_0(s)$ and $\tilde{x}_0(s)$, respectively. Assume that the far field patterns $u^\infty(\hat{x}, \theta, k, D)$ and $u^\infty(\hat{x}, \theta, k, \tilde{D})$ of the two obstacles satisfy*

$$\sup_{\hat{x}\in\mathbb{S}^1} |u^\infty(\hat{x}, \theta, k, D) - u^\infty(\hat{x}, \theta, k, \tilde{D})| \leq \delta.$$

Then, at the high frequency regime we have

$$\left| \frac{1}{\sqrt{\kappa(x_0(s))}} - \frac{1}{\sqrt{\tilde{\kappa}(\tilde{x}_0(s))}} \right| \leq \frac{2\delta}{\sqrt{|\theta - \hat{x}|}} + \frac{1}{\sqrt{\kappa_l}} O(\frac{1}{k|\theta - \hat{x}|}). \tag{54}$$

Proof. It follows from (53) that

$$\frac{1}{\sqrt{\kappa(x_0(s))}} = \frac{2|u^\infty(\hat{x}, \theta, k, D)|}{\sqrt{|\theta - \hat{x}|}} \left[1 + O(\frac{1}{k|\theta - \hat{x}|})\right].$$

A similar equality can be obtained for the obstacle $\tilde{D}$. Subtracting these two equalities, we obtain

$$\left| \frac{1}{\sqrt{\kappa(x_0(s))}} - \frac{1}{\sqrt{\tilde{\kappa}(\tilde{x}_0(s))}} \right| = \frac{2}{\sqrt{|\theta - \hat{x}|}} \left\{ \delta + O(\frac{1}{k|\theta - \hat{x}|}) \left[|u^\infty(\hat{x}, \theta, k, D)| + |u^\infty(\hat{x}, \theta, k, \tilde{D})| \right] \right\} \tag{55}$$

On the other hand, since $\kappa(x_0(s)) \geq \kappa_l$, the far field pattern $u^\infty(\hat{x}, \theta, k, D)$ is bounded by

$$|u^\infty(\hat{x}, \theta, k, D)| \leq \frac{\sqrt{|\theta - \hat{x}|}}{\sqrt{\kappa_l}}$$

for k large enough such that $|1 + O(\frac{1}{k|\theta-\hat{x}|})| < 2$. The same estimate is also true for $|u^\infty(\hat{x}, \theta, \tilde{D})|$. Replacing into (55), we obtain (54). The proof is complete. □

This theorem says that the curvature of the obstacle can be stably reconstructed in the illuminated part. However, the curvature does not determine the obstacle uniquely. For the uniqueness of the reconstruction, we use also the support function $d(s)$. Note that from (53) we can see that $u^\infty(\hat{x}, \theta, k, D) \neq 0$. Dividing (53) by the similar equation for $\tilde{D}$, we have

$$\frac{u^\infty(\hat{x}, \theta, k, D)}{u^\infty(\hat{x}, \theta, k, \tilde{D})} = \sqrt{\frac{\tilde{\kappa}(\tilde{x}_0(s))}{\kappa(x_0(s))}} e^{ik|\theta - \hat{x}|[d(s) - \tilde{d}(s)]} \left[1 + O(\frac{1}{k|\theta - \hat{x}|})\right],$$

where $\tilde{d}$ is the support function of the obstacle $\tilde{D}$. Here, we have used the estimate $\frac{1+O(\frac{1}{k|\theta-\hat{x}|})}{1+O(\frac{1}{k|\theta-\hat{x}|})} = 1 + O(\frac{1}{k|\theta-\hat{x}|})$. We take the logarithm of the both sides to obtain

$$\begin{aligned} \mathrm{Log}\left[\frac{u^\infty(\hat{x}, \theta, k, D)}{u^\infty(\hat{x}, \theta, k, \tilde{D})}\right] = &\log\left[\sqrt{\frac{\tilde{\kappa}(\tilde{x}_0(s))}{\kappa(x_0(s))}}\right] + \mathrm{Log}\left[1 + O(\frac{1}{k|\theta - \hat{x}|})\right] \\ &+ ik|\theta - \hat{x}|[d(s) - \tilde{d}(s)] + 2i\pi m, \end{aligned} \tag{56}$$

where m is an arbitrary integer and Log represents the principle value of the logarithm of complex numbers. In the following, we use the estimate $\mathrm{Log}(1+\xi) = O(\xi)$ for $\xi \in C$ with small modulus. Then, for small noise level δ, we have

$$\mathrm{Log}\left[\frac{u^\infty(\hat{x},\theta,k,D)}{u^\infty(\hat{x},\theta,k,\tilde{D})}\right] = \mathrm{Log}\left[1+\frac{O(\delta)}{u^\infty(\hat{x},\theta,k,\tilde{D})}\right] = O(\frac{\delta}{|u^\infty(\hat{x},\theta,k,\tilde{D})|}).$$

Now we assume that the curvature of the obstacles are bounded, i.e., $\kappa(x_0(s)) \leq \kappa_u$ and $\tilde{\kappa}(\tilde{x}_0(s)) \leq \kappa_u$ for some positive constant κ_u. This condition implies that $|u^\infty(\hat{x},\theta,k,\tilde{D})| \geq \frac{\sqrt{|\theta-\hat{x}|}}{4\sqrt{\kappa_u}}$ for $1+O(\frac{1}{k|\theta-\hat{x}|}) > \frac{1}{2}$. Therefore,

$$\left|\mathrm{Log}\left[\frac{u^\infty(\hat{x},\theta,k,D)}{u^\infty(\hat{x},\theta,k,\tilde{D})}\right]\right| \leq \frac{4\sqrt{\kappa_u}}{\sqrt{|\theta-\hat{x}|}}O(\delta). \tag{57}$$

Similarly,

$$\mathrm{Log}\left[1+O(\frac{1}{k|\theta-\hat{x}|})\right] = O(\frac{1}{k|\theta-\hat{x}|}). \tag{58}$$

Finally, since the first term on the right hand side of (56) is real, taking the imaginary part of the both sides and using (57) and (58), we obtain

$$|d(s)-\tilde{d}(s)| \leq \frac{1}{k|\theta-\hat{x}|}\left\{\frac{4\sqrt{\kappa_u}}{\sqrt{|\theta-\hat{x}|}}O(\delta)+O(\frac{1}{k|\theta-\hat{x}|})\right\}+\frac{2\pi|m|}{k|\theta-\hat{x}|} \tag{59}$$

and

$$|m| \leq \frac{k|\theta-\hat{x}||d(s)-\tilde{d}(s)|}{2\pi}+\frac{1}{2\pi}\left\{\frac{4\sqrt{\kappa_u}}{\sqrt{|\theta-\hat{x}|}}O(\delta)+O(\frac{1}{k|\theta-\hat{x}|})\right\}. \tag{60}$$

In general, the right hand side of (59) can be arbitrary large since m is arbitrary. To reconstruct the support function, Ramm and Gutman used different combinations of θ and $\hat{x}$ to eliminate m, see [14]. In our work, to obtain a good stability estimate for each fixed pair of θ and $\hat{x}$, we propose a condition under which m must be zero. For this purpose, let us assume that the support functions $d(s)$ and $\tilde{d}(s)$ satisfy the condition

$$|d(s)-\tilde{d}(s)| \leq \epsilon\frac{\pi}{k} \tag{61}$$

for a fixed value $\epsilon \in (0,1)$, see Figure 2(b) (ϵ can be taken to be 1 for $\hat{x} \neq -\theta$). Then, from (60) we can see that for δ small enough and k large enough, with the note that $|\theta-\hat{x}| \leq 2$, we have

$$|m| \leq \epsilon+\frac{1}{2\pi}\left\{\frac{4\sqrt{\kappa_u}}{\sqrt{|\theta-\hat{x}|}}O(\delta)+O(\frac{1}{k|\theta-\hat{x}|})\right\} < 1.$$

Thus $m=0$. Replacing this into (59), we obtain the point-wise stability estimate for the support function. We summarize the above results in the following theorem.

Theorem 5.2. *Assume that the support functions $d(s)$ and $\tilde{d}(s)$ of D and $\tilde{D}$ satisfy*

$$d_* \leq d(s) \leq d^*, \quad d_* \leq \tilde{d}(s) \leq d^* \tag{62}$$

with $|d^* - d_*| \leq \epsilon\frac{\pi}{k}$ *for a fixed value* $\epsilon \in (0,1)$*. Then, for* δ *small enough and* k *large enough, we have*

$$|d(s) - \tilde{d}(s)| \leq \frac{4\sqrt{\kappa_u}}{k|\theta - \hat{x}|^{3/2}}O(\delta) + O(\frac{1}{k^2|\theta - \hat{x}|^2}), \tag{63}$$

where κ_u *is the upper bound of the curvature of the obstacles.*

Remark 5.1. *We remark that the condition* (61) *is natural since if it is not satisfied, the uniqueness of the inverse obstacle scattering problem can not be guaranteed in general and, therefore, the stability estimate* (59) *is meaningless.*

From Theorem 5.1 and Theorem 5.2 we can conclude that if the observable shape $D(\tilde{r}(k_h))$ satisfies the condition (61) compared with the exact shape, its curvature and support function approximate well those of the exact shape in the illuminated part. However, as shown in (54) and (63), the stability depends on the angle between θ and $\hat{x}$. The best stability is obtained at $\hat{x} = -\theta$, i.e., at the specular point $x_0(\theta)$, and the higher the angle between θ and $\hat{x}$, the worse the stability. Near the two ends of the illuminated part ∂D_+, $|\theta - \hat{x}|$ becomes very small which makes the expansion (53) useless. The theorems do not say anything about the reconstruction accuracy in the shadowed part of the obstacle's boundary in the high frequency regime.

Note that, we can also obtain stability estimates in the L^2-norm as follows. For a fixed value $\gamma \in (0,2)$, we denote by $\hat{x}_1$ and $\hat{x}_2$ the directions such that $|\theta - \hat{x}_j| = \gamma$. We also denote by $s_j := \frac{\theta - \hat{x}_j}{|\theta - \hat{x}_j|}, j = 1,2$, and $\mathbb{S}^1_\gamma \subset \mathbb{S}^1$ the set of directions s between s_1 and s_2 (the directions associated with the solid curves in Figure 2(b), or equivalently, with the observation angles $\hat{x}$ such that $|\theta - \hat{x}| \geq \gamma$). Then, buy integrating the estimate (63) with respect to s over this set, we obtain

$$\|d - \tilde{d}\|_{L^2(\mathbb{S}^1_\gamma)} \leq \frac{4\sqrt{2\pi\kappa_u}}{k\gamma^{3/2}}O(\delta) + O(\frac{1}{k^2\gamma^2}). \tag{64}$$

For obstacles whose shapes are not strictly convex, the above point-wise stability estimates can still be obtained for its convex illuminated part provided that the shape satisfies some conditions as described by Alber and Ramm [1]. Under these conditions, the Kirchhoff approximation is still valid and we can use the above analysis for the convex illuminated part.

Finally, given the support function, the illuminated part of the obstacle can be stably reconstructed with the accuracy of $O(\sqrt{\delta d})$, where δd is the error of the support function, see [14].

6 Numerical results and discussion

The analysis of the previous sections suggests that, given the measured far field patterns at a set of frequency, the reconstruction of the obstacle should be done as follows: we choose an initial guess in the set of convexity $B(\frac{\pi}{k_l})$ of the least-squares objective functional at the lowest frequency and estimate an approximation r_0 of $\tilde{r}(k_l)$ using a gradient-based optimization method. Then the approximation is updated using the RLA. In this section, we show some

numerical examples to illustrate the theoretical results in the previous sections. That is, (i) the choice of the lowest frequency and initial guesses; (ii) the effect of the number of frequencies on the convergence of the RLA; and (iii) the accuracy at the highest frequency.

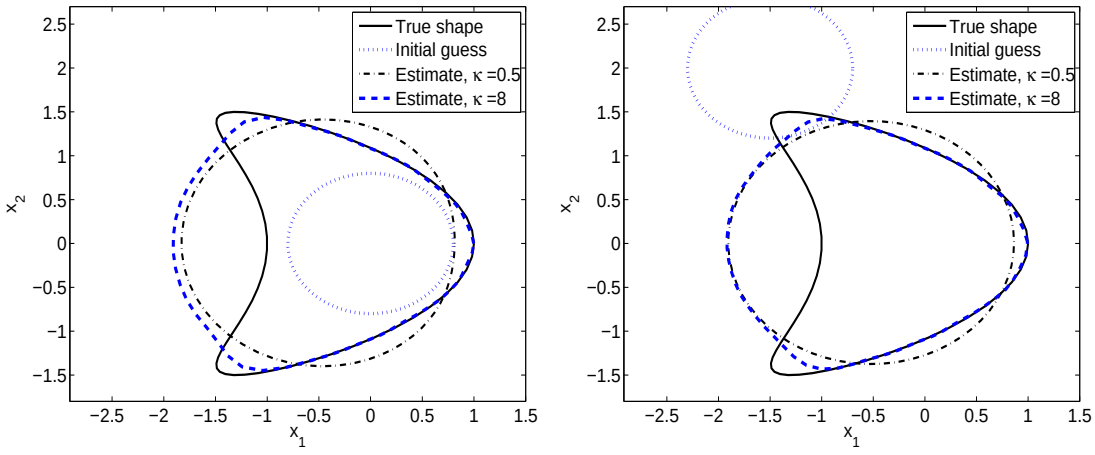

(a) (b)

Figure 3: Reconstruction of the kite with different initial guesses: (a) $|x| = 0.8$; (b) $|x - (-1.5, 2)| = 0.8$.

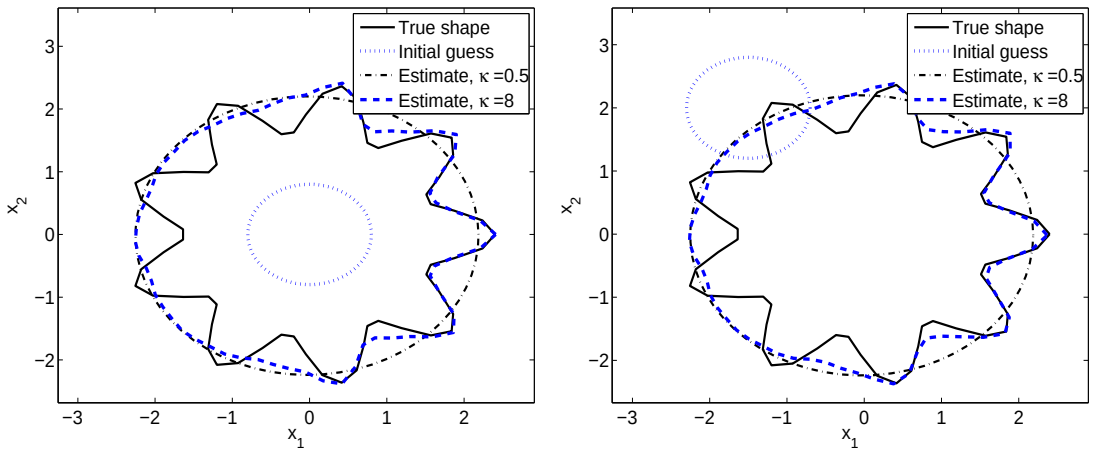

(a) (b)

Figure 4: Reconstruction of the flower with different initial guesses: (a) $|x| = 0.8$; (b) $|x - (-1.5, 2)| = 0.8$..

In the following examples, we consider two obstacles. The first one is a kite-shaped domain of which the boundary is given by $\{x(t) = (\cos t + 0.65(\cos 2t - 1), \sin t), t \in [0, 2\pi)\}$. The second one is a flower-shaped obstacle defined by the equation $\{x(t) = c_1(1 + c_2 \cos c_3 t)(\cos t, \sin t), t \in [0, 2\pi)\}$ with positive constants c_1, c_2 and c_3. The first parameter determines the area of the obstacle, the second one relates to the curvature and the last one determines the number of

petals of the "flower". In the following tests, these parameters were set to be $c_1 = 2$, $c_2 = 0.2$, and $c_3 = 9$.

The measured far field patterns $u_m^\infty(\cdot, k_j, r)$, $j = 0, \ldots, N$, used in these tests were simulated as the solution of the forward problem (1)–(3) which was solved by the integral equation method [10]. We used 16 observation directions uniformly distributed on the unit circle. The same method was also used to calculate the domain derivative of the far field operator. For simulating measurement noise, we added 5% random noise to the measured far field patterns.

The regularization parameter α was chosen to be 10^{-2}. We note that this parameter need not be dependent on the noise level. Using numerical tests, we have heuristically found that α can be chosen in a wide range, says, from 10^{-6} to 10^{-1} which still gives good reconstruction results.

Let us first analyze the effect of the choice of the lowest frequency and initial guesses on the convergence and accuracy of the algorithm. Here we fix the direction of incidence to be $\theta = (-1, 0)$. We show in Figure 3 two estimates of the kite using $N = 24$ wavenumbers between 0.5 and 8. The approximation r_0 at the lowest frequency was calculated by solving the least-squares nonlinear problem with only three unknowns β_0, β_1 and γ_1 using the Matlab optimization routine *fmincon*. For this nonlinear minimization problem, two different initial guesses were chosen. In Figure 3(a), the algorithm was started at $\{|x| = 0.8\}$ and in Figure 3(b) the initial guess was chosen to be $\{|x - (-1.5, 2)| = 0.8\}$. Note that in this case, the interior point x^0 of the obstacle in the representation (5) could not be chosen as the center of the initial guess circle. In order to find an interior point of the real obstacle, we updated the center of the initial guess after each run of the inverse problem at the lowest frequency. Then it was run again at the lowest frequency with the new initial guess which is also a circle of the same radius as the original initial guess but with the updated center. The update was done for a few times until the center could not be significantly improved. Then the RLA was started.

From the figure we see clearly that the estimates at the lowest frequency of the two tests are almost the same. This is due to the fact that the two initial guesses are in the domain of convexity of the objective functional. Consequently, the RLA gives similar estimates at the highest frequency. Moreover, these estimates approximate well the exact shape in the illuminated part. However, the approximation is not accurate in the shadowed part. Similar results were also obtained for the flower, see Figure 4.

If the lowest frequency k_l is chosen higher, care must be taken in choosing the initial guesses to guarantee the convergence of the algorithm because the domain of local convexity of the objective functional is reduced.

Next, we show that the performance of the algorithm is affected by the number of frequencies. Theorem 4.5 says that the more frequencies are used, the better the reconstruction should be. To show this, we plot in Figure 5 the results using only 8 frequencies instead of 24 as in the previous tests. Figure 5(a) shows that the reconstruction of the kite is still good. This is probably due to its regular illuminated part. However, the reconstruction of the flower is poor as shown in

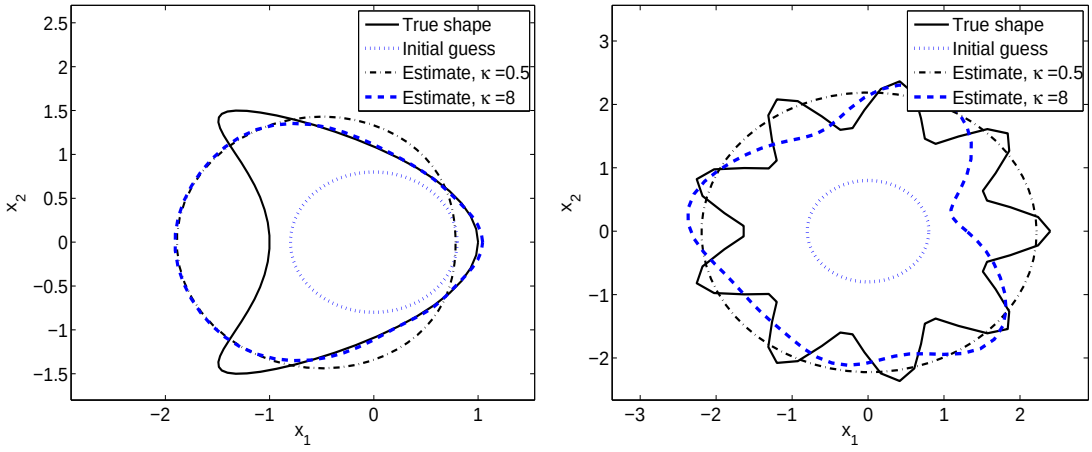

(a) (b)

Figure 5: Effect of the number of frequencies, $N = 8$: (a) The kite; (b) The flower.

Figure 5(b).

Finally, let us analyze the reconstruction accuracy at the highest frequency. We have shown in Figures 3 and 4 that the reconstruction of the obstacles are accurate in the illuminated part, even for the non-convex flower. However, if we reduce the highest frequency, small details should be lost. Indeed, Figure 6 shows the reconstruction results of the obstacles with the highest wavenumber $k_h = 4$. In these runs, we also used the same number of frequencies $N = 24$. It is shown that the kite was reconstructed with almost the same accuracy as with $k_h = 8$ due to its regular shape. However, the details of the flower were not well reconstructed (compare Figure 6(b) with Figure 4). That means, small details can be reconstructed only using high frequencies.

7 Conclusions and perspectives

In conclusion, the RLA can produce accurate reconstructions of the obstacles from a very rough initial guess with the condition that the frequencies should be chosen appropriately, say, the lowest frequency should be small enough (depending on the problem under consideration), the highest frequency and the number of intermediate frequencies should be large. For sound-soft obstacles, we obtained an upper bound for the lowest frequency so that the objective functional is convex in a given region.

The following points are some perspectives for the near future. Firstly, we want to obtain explicit estimates of the constants $d_j, j = 1 \dots 5$, of (23) using Theorem 2.1 and the results of [15]. Secondly, we want to estimate an approximation of the singular value σ by replacing the observable shape at each frequency by the corresponding solution of the RLA. Combining this with the estimates of the constants $d_j, j = 1 \dots 5$, will enable us to verify the condition (45). Thirdly, to improve the convergence rate of the algorithm, higher order approximations should

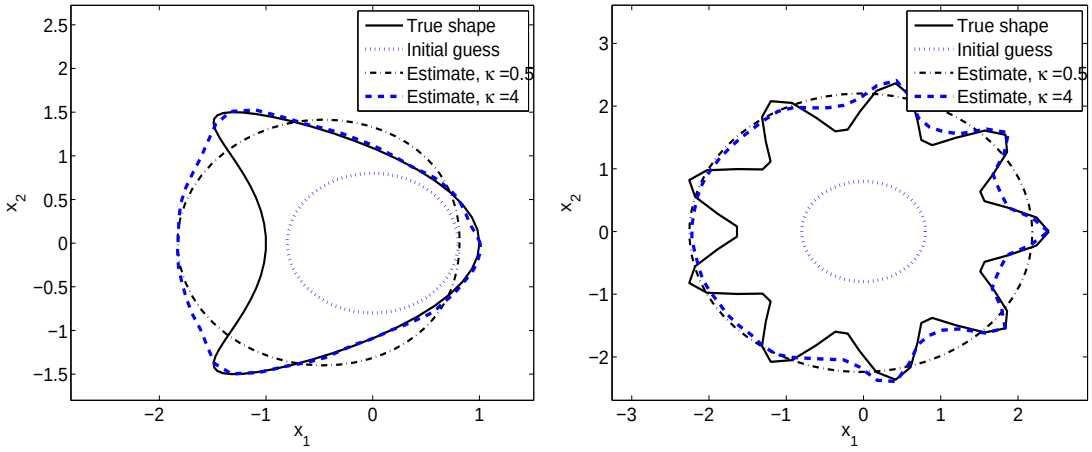

Figure 6: Effect of the highest frequency, $k_h = 4$: (a) The kite; (b) The flower.

be used. Finally, we want to extend this type of algorithms for multiple obstacles. In this case, the reconstruction accuracy could be improved in some shadowed part due to the multiple scattering between the obstacles.

Acknowledgements

This work was supported by the Johann Radon Institute for Computational and Applied Mathematics (RICAM), Austrian Academy of Sciences and by the Austrian Science Fund (FWF) under the project No. P22341-N18. The authors would like to thank V. Isakov and T. Hohage for discussions concerning this work.

References

[1] H.-D. Alber and A. G. Ramm. Scattering amplitude and algorithm for solving the inverse scattering problem for a class of nonconvex obstacles. *J. Math. Anal. Appl.*, 117(2):570–597, 1986.

[2] G. Alessandrini and L. Rondi. Determining a sound-soft polyhedral scatterer by a single far-field measurement. *Proc. Amer. Math. Soc.*, 133(6):1685–1691 (electronic), 2005.

[3] H. Ammari, J. Garnier, H. Kang, M. Lim, and K. Sølna. Multistatic imaging of extended targets. *SIAM J. Imaging Sci.* To appear.

[4] G. Bao and F. Triki. Error estimates for the recursive linearization of inverse medium problems. *Journal of Computational Mathematics*, 28(6):725–744, 2010.

[5] O. Bucci, L. Crocco, T. Isernia, and V. Pascazio. Inverse scattering problems with multi-frequency data: reconstruction capabilities and solution strategies. *IEEE Transactions on Geoscience and Remote Sensing*, 38(4):1749–1756, 2000.

[6] F. Cakoni and D. Colton. *Qualitative Methods in Inverse Scattering Theory.* Springer, 2006.

[7] Y. Chen. Inverse scattering via Heisenberg's uncertainty principle. *Inverse Problems*, 13(2):253–282, 1997.

[8] J. Cheng and M. Yamamoto. Global uniqueness in the inverse acoustic scattering problem within polygonal obstacles. *Chinese Ann. Math. Ser. B*, 25(1):1–6, 2004.

[9] W. Chew and J. Lin. A frequency-hopping approach for microwave imaging of large inhomogeneous bodies. *IEEE Microwave and Guided Wave Letters*, 5:439–441, 1995.

[10] D. Colton and R. Kress. *Inverse acoustic and electromagnetic scattering theory.* Springer-Verlag, Berlin, second edition, 1998.

[11] D. Colton and B. D. Sleeman. Uniqueness theorems for the inverse problem of acoustic scattering. *IMA J. Appl. Math.*, 31(3):253–259, 1983.

[12] G. B. Folland. *Fourier analysis and its applications.* The Wadsworth & Brooks/Cole Mathematics Series. Wadsworth & Brooks/Cole Advanced Books & Software, Pacific Grove, CA, 1992.

[13] D. Gintides. Local uniqueness for the inverse scattering problem in acoustics via the Faber-Krahn inequality. *Inverse Problems*, 21(4):1195–1205, 2005.

[14] S. Gutman and A. G. Ramm. Support function method for inverse obstacle scattering problems. In *Acoustics, mechanics, and the related topics of mathematical analysis*, pages 179–184. World Sci. Publ., River Edge, NJ, 2002.

[15] F. Hettlich and W. Rundell. A second degree method for nonlinear inverse problems. *SIAM J. Numer. Anal.*, 37(2):587–620 (electronic), 2000.

[16] N. Honda, G. Nakamura, and M. Sini. Analytic extention and reconstruction of obstacles from few measurements for elliptic second order operators. Preprint.

[17] L. Hörmander. *The analysis of linear partial differential operators I. Distribution theory and Fourier analysis.* Springer-Verlag, Berlin, 2003. Reprint of the second (1990) edition.

[18] V. Isakov. *Inverse problems for partial differential equations.* Springer, New York, second edition, 2006.

[19] A. Kirsch. The domain derivative and two applications in inverse scattering theory. *Inverse Problems*, 9(1):81–96, 1993.

[20] A. Kirsch and N. Grinberg. *The factorization method for inverse problems*, volume 36 of *Oxford Lecture Series in Mathematics and its Applications*. Oxford University Press, Oxford, 2008.

[21] R. Kress. Newton's method for inverse obstacle scattering meets the method of least squares. *Inverse Problems*, 19(6):S91–S104, 2003.

[22] W. McLean. *Strongly elliptic systems and boundary integral equations*. Cambridge University Press, Cambridge, 2000.

[23] R. Potthast. A survey on sampling and probe methods for inverse problems. *Inverse Problems*, 22(2):R1–R47, 2006.

[24] A. G. Ramm. *Multidimensional inverse scattering problems*. Longman Scientific & Technical, Harlow, 1992.

[25] E. Sincich and M. Sini. Local stability for soft obstacles by a single measurement. *Inverse Probl. Imaging*, 2(2):301–315, 2008.

[26] P. Stefanov and G. Uhlmann. Local uniqueness for the fixed energy fixed angle inverse problem in obstacle scattering. *Proc. Amer. Math. Soc.*, 132(5):1351–1354 (electronic), 2004.